



## Original Paper

# Research on the solid particle erosion wear of pipe steel for hydraulic fracturing based on experiments and numerical simulations



Si-Qi Yang<sup>a, b</sup>, Jian-Chun Fan<sup>b, \*</sup>, Ming-Tao Liu<sup>c</sup>, De-Ning Li<sup>d</sup>, Jun-Liang Li<sup>e</sup>,  
Li-Hong Han<sup>a, \*\*</sup>, Jian-Jun Wang<sup>a</sup>, Shang-Yu Yang<sup>a</sup>, Si-Wei Dai<sup>b</sup>, Lai-Bin Zhang<sup>b</sup>

<sup>a</sup> State Key Laboratory of Oil and Gas Equipment, CNPC Tubular Goods Research Institute, Xi'an, 710077, Shaanxi, China

<sup>b</sup> Key Laboratory of Oil and Gas Safety and Emergency Technology, China University of Petroleum, Beijing, 102249, China

<sup>c</sup> Oil Production Technology Research Institute of Liaohe Oilfield Company, Panjin, 124010, Liaoning, China

<sup>d</sup> Tianjin Gas Storage Branch, PetroChina Dagang Oilfield Company, Tianjin, 300280, China

<sup>e</sup> Petroleum Production Engineering Research Institute, Daqing Oilfield Company, Daqing, 163712, Heilongjiang, China

## ARTICLE INFO

## Article history:

Received 16 May 2023

Received in revised form

8 January 2024

Accepted 22 March 2024

Available online 26 March 2024

Edited by Jie Hao and Meng-Jiao Zhou

## Keywords:

Erosion wear

Applied stress

Particle impact dynamics

Erosion mechanism

## ABSTRACT

Erosion wear is a common failure mode in the oil and gas industry. In the hydraulic fracturing, the fracturing pipes are not only in high-pressure working environment, but also suffer from the impact of the high-speed solid particles in the fracturing fluid. Beneath such complex conditions, the vulnerable components of the pipe system are prone to perforation or even burst accidents, which has become one of the most serious risks at the fracturing site. Unfortunately, it is not yet fully understood the erosion mechanism of pipe steel for hydraulic fracturing. Therefore, this article provides a detailed analysis of the erosion behavior of fracturing pipes under complex working conditions based on experiments and numerical simulations. Firstly, we conducted erosion experiments on AISI 4135 steel for fracturing pipes to investigate the erosion characteristics of the material. The effects of impact angle, flow velocity and applied stress on erosion wear were comprehensively considered. Then a particle impact dynamic model of erosion wear was developed based on the experimental parameters, and the evolution process of particle erosion under different impact angles, impact velocities and applied stress was analyzed. By combining the erosion characteristics, the micro-structure of the eroded area, and the micro-mechanics of erosion damage, the erosion mechanism of pipe steel under fracturing conditions was studied in detail for the first time. Under high-pressure operating conditions, it was demonstrated through experiments and numerical simulations that the size of the micro-defects in the eroded area increased as the applied stress increased, resulting in more severe erosion wear of fracturing pipes.

© 2024 The Authors. Publishing services by Elsevier B.V. on behalf of KeAi Communications Co. Ltd. This is an open access article under the CC BY-NC-ND license (<http://creativecommons.org/licenses/by-nc-nd/4.0/>).

## 1. Introduction

Erosion wear caused by solid particles has garnered widespread attention due to the fact that it is a crucial cause of material failure in many industries. In the oil and gas production, the particles entrained by the flowing liquid or gas constantly impinge upon the pipe walls at a particular angle and velocity, causing erosion wear damage to the pipeline system, particularly in elbows, valves, and tees. The severe erosion damage may lead to equipment failure and

fluid leakage. Hydraulic fracturing is an important measure to increase production. During the hydraulic fracturing operation, the ceramic proppants entrained in the high-pressure fracturing fluid are transported from the ground to the downhole to keep the cracks open, thus helping oil or gas to flow more freely. In this case, the fracturing pipes carrying the high-pressure sand-laden fluid are subjected to the high-speed impact of solid particles within the tube, in addition to significant stress caused by high operating pressures (sometimes exceeding 100 MPa) (Yang and Gao, 2022; Josifovic et al., 2016). Beneath these coupling working conditions, vulnerable components in the pipe system, such as elbows, tees, and valves, are susceptible to extremely severe erosion wear that may shorten their service life (Wang et al., 2020; Yao et al., 2023; Zhang et al., 2019). Once the pipe ruptures due to erosion damage,

\* Corresponding author.

\*\* Corresponding author.

E-mail addresses: [fjc19090@126.com](mailto:fjc19090@126.com) (J.-C. Fan), [hanlihong@cnpcc.com.cn](mailto:hanlihong@cnpcc.com.cn) (L.-H. Han).

the high-pressure fluid flowing in the pipe fittings leaks, posing a serious threat to personnel safety and equipment integrity.

The severity of erosion wear is non-linearly affected by numerous factors, and the relationship between these factors is nonlinear. Although not all the factors that affect erosion wear have been identified, for slurry erosion, the main factors can be categorized into four categories: impact conditions (such as impact velocity, impact angle, impact level, and wet/dry conditions), particle characteristics (such as shape, size, hardness, and composition), slurry characteristics (such as concentration, temperature, viscosity, corrosivity, and flow pattern), and target material characteristics (such as hardness, toughness, corrosion resistance, and yield strength) (Parsi et al., 2014; Javaheri et al., 2018; Wang et al., 2019b). Among these factors, flow velocity and impact angle are considered to be the most critical. Yoganandh et al. (2013) conducted orthogonal erosion tests on four influencing factors, including flow velocity, impact angle, slurry concentration, and particle size. The results showed that the contribution of flow velocity and impact angle to the erosion wear of the materials was 60% and 21%, respectively. In regard to impact velocity, the higher the impact velocity of a particle, the higher its kinetic energy when impacting the target material (Parsi et al., 2014; Huang et al., 2008; Nguyen et al., 2014; Al-Bukhaiti et al., 2007; Abedini and Ghasemi, 2014). Sufficient experimental studies have shown that there is a power function relationship between the erosion wear rate and the impact velocity (Akbarzadeh et al., 2012; Oka et al., 2005; Ahlert, 1994; Alam et al., 2016):

$$ER \propto (u^P)^n \quad (1)$$

where  $ER$  is the erosion wear of target material,  $u^P$  represents the particle impact velocity,  $n$  is a power exponent. The value of  $n$  is an empirical coefficient that varies considerably with the properties of impacting particles and the target materials, and the value of this coefficient generally varies between 1.7 and 2.6 for ductile metallic materials (Oka et al., 2005; Sapate and RamaRao, 2003; Islam et al.,

2016).

In terms of impact angle, most studies have found that for ductile materials, the erosion wear rate increases first and then decreases with the increase of impact angle (Al-Bukhaiti et al., 2007; Liu et al., 2021; Zhang et al., 2021). It has been observed that the impact angles causing the most severe erosion wear generally occur between 20° and 40° (Abedini and Ghasemi, 2014; Abbade and Crnkovic, 2000; Zhang et al., 2016). The relationship between impact angle and erosion wear rate can be approximately expressed by a higher order polynomial (Ahlert, 1994; Veritas, 2007; Zhang et al., 2007; McLaury and Shirazi, 2000).

Although numerous experimental studies have been committed to investigating the influential mechanism of various parameters on erosive wear, almost all erosion tests in the existing literature were carried out at approximately atmospheric pressure without considering the effect of applied stress. However, in the oil and gas field, almost all equipment must be subjected to applied stress caused by internal pressure or external load during the service period, such as the fracturing pipes. Surprisingly, only a few related studies involving high applied stress have been conducted. Cao et al. (2022) conducted two-phase gas-solid particle jet erosion tests on 316L stainless steel under different tensile stress and different erosion angles. They found that in the elastic range, the erosion rate manifests a rising trend with the increase of stress. Wang et al. (2022) proposed a testing method for free fall coarse particle stress-erosion, and the erosion behavior of stainless steel SS304 under different loads and impact angles was experimentally studied. Through this method, the stress-acceleration effect of stainless steel SS304 has been found. In addition, in our previous studies, we carried out the experimental studies of solid particle erosion that took into account tensile stress and found that it may play a crucial role in aggravating the erosion wear rate (Sun et al., 2015; Yang et al., 2021). Based on the stress-erosion tests data, some researchers have established the fit model about the stress-accelerated erosion (Yang et al., 2021; Xu et al., 2022; Wang et al., 2019a). Although the exacerbating effect of applied stress on the

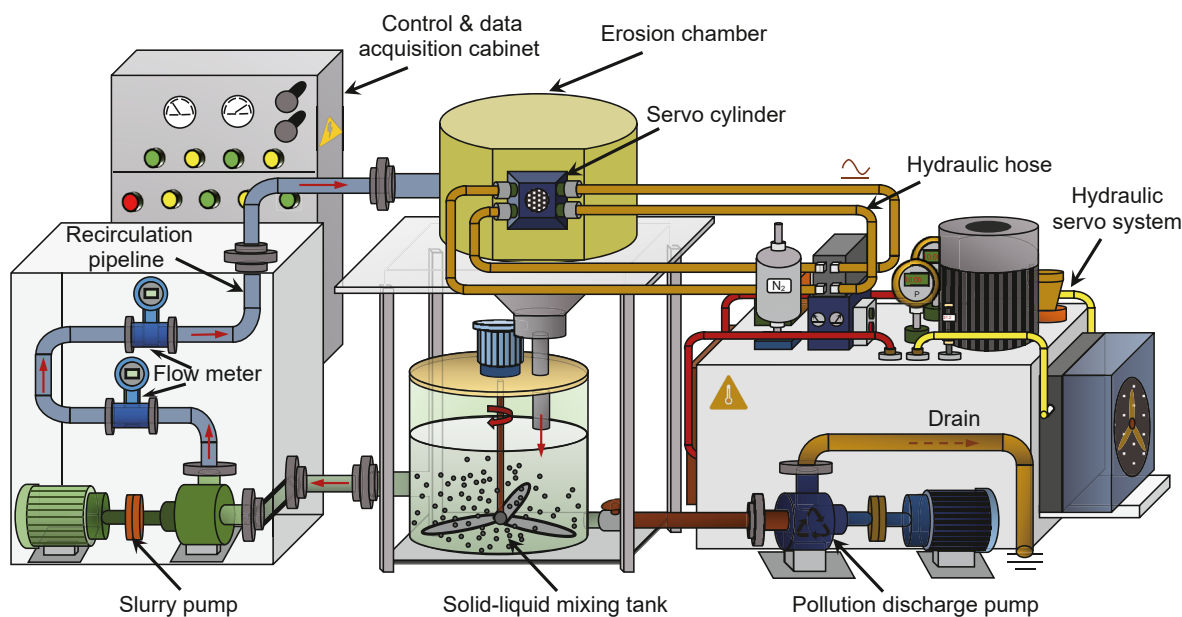
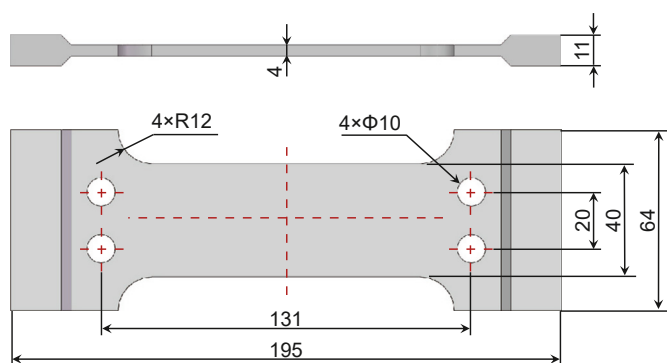


Fig. 1. Schematic diagram of the erosion testing system.

**Table 1**  
Mechanical properties and nominal chemical composition of AISI 4135 steel.

(a) Mechanical properties of AISI 4135 steel									
Density, kg/m <sup>3</sup>	Yield strength, MPa	Tensile strength, MPa	Elastic modulus, GPa	Brinell hardness	Reduction of area	Extensibility			
7850	835	985	207	229	45%	≥12%			
(b) Nominal chemical composition of AISI 4135 steel									
	C	Si	Mn	Cr	Mo	P	S	Ni	Cu
wt%	0.33–0.38	0.15–0.35	0.70–0.90	0.80–1.10	0.15–0.25	≤0.035	≤0.040	≤0.030	≤0.030



**Fig. 2.** Schematic representation of the testing specimen. (unit: mm).

erosion wear of ductile metals has been observed, the erosion mechanism of stress-erosion of the target material has not been effectively revealed yet, which makes it difficult for researchers to grasp the erosion behavior of pipe steel for hydraulic fracturing under complex coupling conditions, and may lead to flaws in fracturing pipes design and maintenance.

In addition to experimental studies, many researchers were committed to the implementation of numerical simulation to

analyze the erosion mechanism. At present, most studies focus on the analysis of erosion prediction based on computational fluid dynamics (CFD) methods. Duarte and Souza (2017) performed numerical simulations of gas-solid erosion of elbows and analyzed the effect of structural parameters on erosion wear to mitigate elbow erosion. Parsi et al. (2015, 2017) carried out a CFD simulation of solid particle erosion in gas-dominant multiphase flow, reported that the maximum erosion occurred at the top of elbow extrados, and investigated the effects of particle velocity, particle distribution and particle size on the erosion mechanism. Zhu et al. (Zhu and Qi, 2019; Zhu et al., 2015) performed a series of CFD simulations of solid particle erosion for the pipe fittings such as elbows and tees in oil and gas pipeline systems, analyzing the effects of flow velocity, particle size, and structure characteristics on erosion wear. However, there were relatively few numerical simulations to study the erosion mechanism of solid particles on target materials from the perspective of impact dynamics. Shimizu et al. (1999, 2000) studied the dependency on impact angle during erosion wear using a two-dimensional single-particle impact model. Chen and Li (2003) constructed a dynamic two-dimensional computational model based on Newton's law of motion to simulate the surface damage of composite materials caused by solid particle erosion. Zang et al. (2022) carried out the numerical simulations to investigate the wear morphology and stress distribution of a target material

**Table 2**  
Mechanical properties and nominal chemical composition of the ceramsite sand.

(a) Mechanical properties of ceramsite sand								
Density, kg/m <sup>3</sup>	Average size, μm	Sphericity	Roundness	Mohs hardness	Breakage rate, %			
1800	400	0.9	0.9	8	86 MPa ≤ 8			
(b) Nominal chemical composition of ceramsite sand								
	Al <sub>2</sub> O <sub>3</sub>	SiO <sub>2</sub>	Fe <sub>2</sub> O <sub>3</sub>	TiO <sub>2</sub>	MnO	K <sub>2</sub> O	CaO	Others
wt%	65.82	14.94	9.43	3.88	2.94	0.85	0.77	1.37

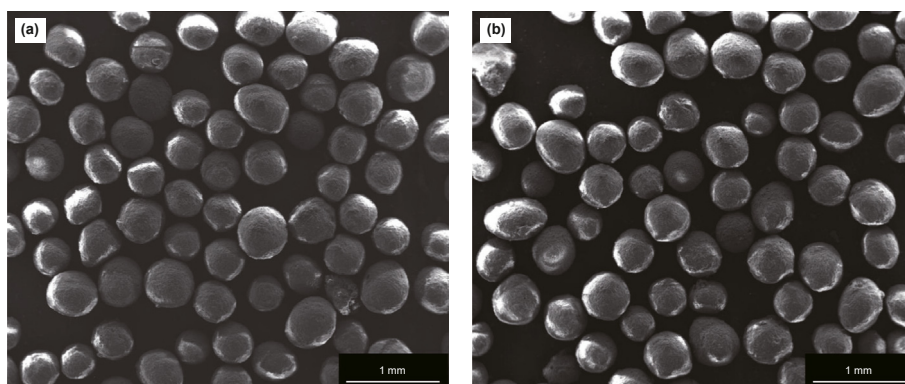


**Fig. 3.** SEM micrographs of the impacting particles before and after the test. (a) Before the test, (b) after the test.

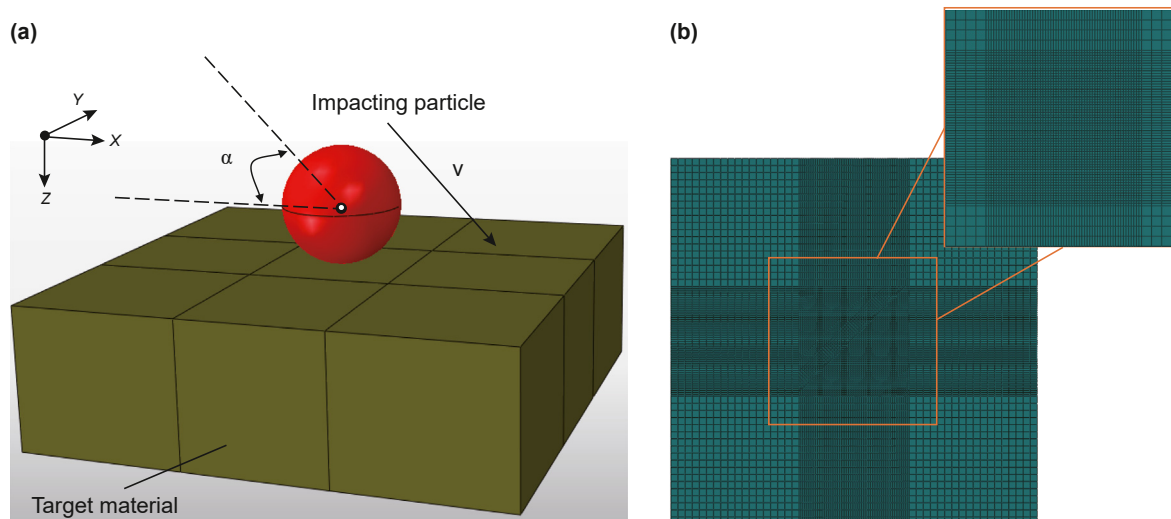


Fig. 4. Geometric model and computational grid division.

Table 3

Mesh-independence test: the maximum Von Mises stress (impact angle = 30°; impact velocity = 20 m/s; applied stress = 0).

Mesh	Number of refined elements	Number of coarse elements	Total number of elements	Von Mises stress, MPa	Percentage change
M1	49392	277200	326592	638.9	/
M2	105903	328104	434007	738.8	13.52%
M3	183708	372960	556668	817.7	9.65%
M4	282807	411768	694575	864.5	5.41%
M5	403200	444528	847728	881.0	1.87%
M6	1552887	793800	2346687	889.2	0.92%

subjected to rotating particle impacts. They found that the rotation of particles impacting a material can significantly affect the magnitude and pattern of impact wear. Hadavi et al. (2016a, 2016b) developed a high-speed impact model of SiC particles using coupled EFG–SPH technique and investigated the effects of incident angle, velocity and abrasive size on the erosion damage, and well predicted the fragmentation and fracture of impacting particles during the erosion wear. From the existing literature on particle impact dynamics, it can be seen that the current research in the field is mainly devoted to the impacting particle properties, such as impact velocity, impact angle and particle rotation, etc. However, few studies have combined the erosion damage micro-mechanics obtained from numerical simulations with the erosion characteristics obtained from experimental studies to reveal the complex erosion mechanism in detail. In addition, the erosion mechanics analysis mentioned in the current literature only considered the contact effect between the impacted particles and the target material, and no study has yet considered the stress state of target material when subjected to particle impact. Therefore, to date there is no study that analyzes erosion wear involving applied stress from the perspective of micro-mechanical. Until now, the complex erosion behavior for fracturing pipes has been a largely under researched domain.

Consequently, in this study, the experimental investigation of solid particle erosion on AISI 4135 steel for fracturing pipes was carried out. Additionally, according to experiments parameters, a particle impact dynamic model of erosion wear was developed using the ABAQUS software. The effects of impact angle, particle velocity and applied stress on the erosion wear were comprehensively analyzed through experiments and numerical simulations. Furthermore, the erosion mechanism of pipe steel under complex fracturing conditions was revealed based on microstructure

characterization and surface deformation micro-mechanics.

## 2. Experimental method

### 2.1. Experimental setup

All experiments were carried out on a novel slurry jet erosion testing system, which can exert controllable tensile load to the testing specimen during the erosion wear. The schematic diagram of the erosion testing apparatus is shown in Fig. 1. The whole erosion testing system included the erosion chamber, hydraulic servo system, solid-liquid mixing tank (approximately 120 L), slurry pump, recirculation pipeline (DN50) and control&data acquisition cabinet. The erosion chamber is the critical component of the whole erosion testing system, consisting of servo cylinder (MOB, Taiking Hydraulic Co., Ltd., China), testing specimen, spray nozzle and tension sensor (SES, Transform Technology Co., Ltd., China). Both sides of the specimen were connected with a servo cylinder and a tension sensor respectively, which can be continuously to tensile stress during the erosion tests. In addition, an angle adjustment device was installed on one side of the specimen, so that the orient angle of specimen can be adjusted between 0° and 90° with the incoming slurry jet direction.

### 2.2. Materials

The target material utilized in this study was AISI 4135 steel, a widely used pipe steel for hydraulic fracturing due to its superior mechanical properties. The mechanical properties and nominal chemical composition of this alloy steel are presented in Table 1. Fig. 2 illustrates the geometric schematic of the specimen used for the erosion tests. The spherical ceramsite sand was served as the

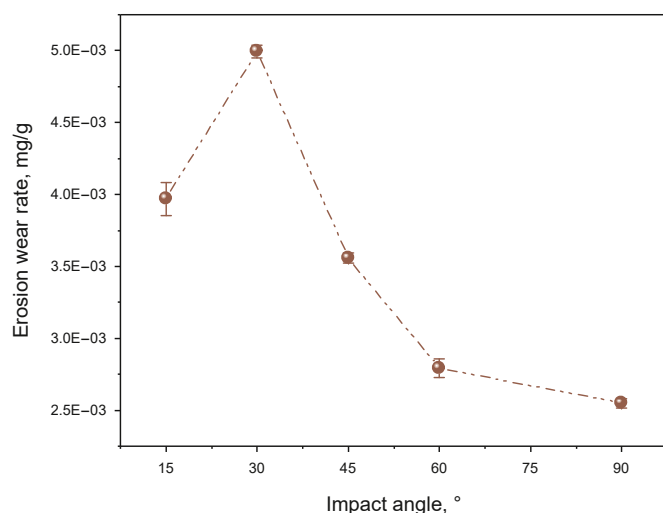


**Fig. 5.** Erosion rates at different impact angles (flow velocity = 15 m/s, applied stress = 0 MPa).

erodent in all the experiments, as it is commonly used in actual hydraulic fracturing conditions. The mechanical properties and nominal chemical composition of the ceramicsite sand are shown in Table 2. Prior to the test, use a fine sieve with specific mesh size to sieve the ceramic sand particles to a size range of 300–500  $\mu\text{m}$ . The SEM micrographs of the impacting particles before and after the test are shown in Fig. 3, indicating that due to the high hardness and non-friable of the ceramicsite sand, the shape and size of the particles did not change significantly before and after the test.

### 2.3. Experimental procedure

During the test, the solid particles were thoroughly mixed with water in the solid-liquid mixing tank at a particle concentration of 10% (in wt%). The resulting sand-laden fluid flowed through a pipeline and impacted the testing specimen via a nozzle. In the experiments, a boron carbide nozzle with an inner diameter of 8 mm was selected, and the outlet portion included a 77 mm long straight cylindrical passage to minimize the dispersion effect of the slurry. The distance between the nozzle outlet and the specimen was 20 mm. The impact angles of particles were respectively set as 15°, 30°, 45°, 60° and 90°. The flow velocities of impact slurry flow were measured by two flow meters (8800 Series, Rosemount Co., Ltd., USA), where the values were set as 5, 10, 15, 20 and 25 m/s, respectively. After impacting the testing specimen, the sand-laden fluid returned to the solid-liquid mixing tank to complete a closed-loop cycle. To ensure a constant particle concentration during the test, we regularly detected the particle concentration through the sample port at the solid-liquid mixing tank. When there was a decrease in particle concentration, we promptly added appropriate solid particles to the solid-liquid mixing tank to maintain a particle concentration of 10%. The testing specimen was subjected to axial tensile stress while being eroded by slurry flow, the tensile stresses were obtained by dividing the tensile force by the cross-sectional area of the testing specimens (160 mm<sup>2</sup>), and the applied stresses were set as 0, 100, 300, and 500 MPa, respectively. All experiments were repeated independently at least three times and the experimental period was 60 min. The laboratory temperature was between 25 and 30 °C. In order to improve the accuracy of experimental data, each specimen was ultrasonically cleaned and dried by hot air blower before and after the test. Mass of each specimen was measured accurately in a high-precision electronic

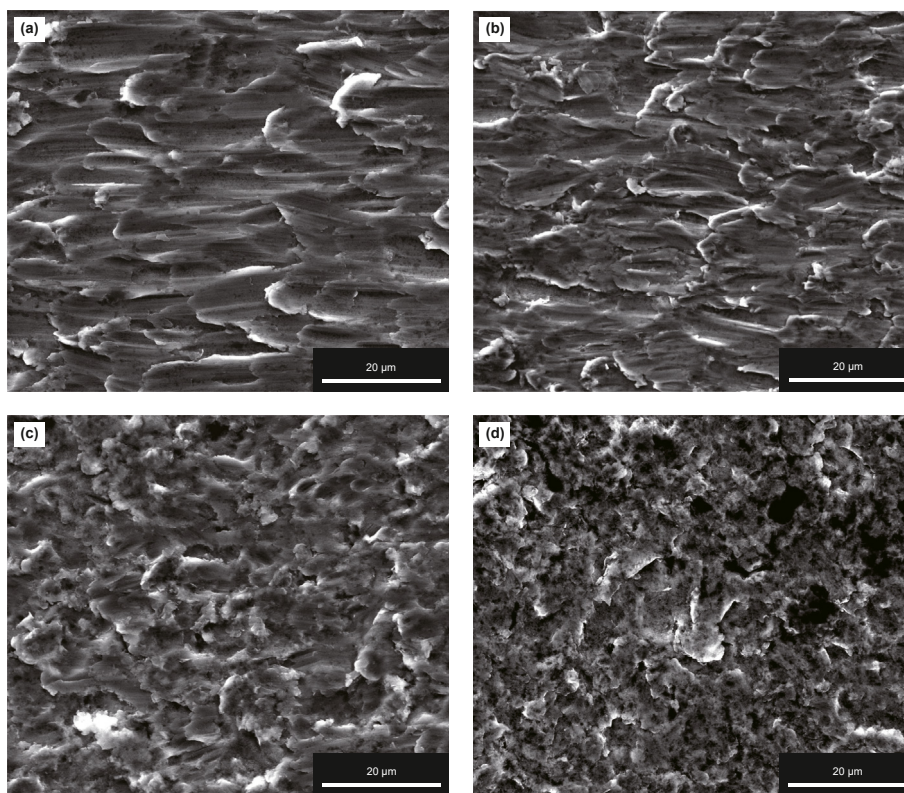


**Fig. 6.** SEM micrographs of the eroded region at different impact angles. (a) impact angle = 15°, (b) impact angle = 30°, (c) impact angle = 60°, (d) impact angle = 90° (flow velocity = 15 m/s, applied stress = 0 MPa).

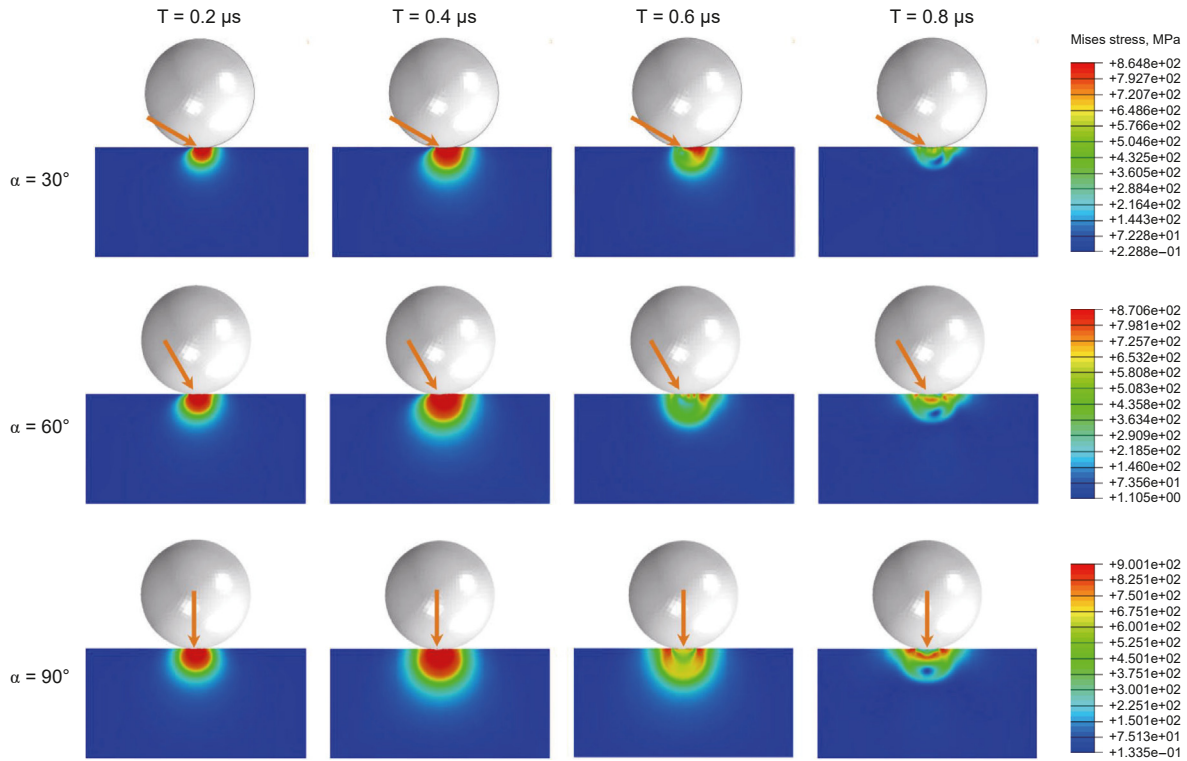


Fig. 7. Equivalent contact stress nephograms of the surface and sub-surface of target material at three impact angles (flow velocity = 15 m/s, applied stress = 0 MPa).

balance (MS104TS/02, Mettler Toledo Inc., Switzerland) with a minimum resolution of 0.1 mg. The erosion rates were defined by the ratio of the mass loss of specimens (in mg) to the mass of impacting solid particles (in g). The ceramicsite sand and water were replaced after each test.

### 3. Finite element analysis

The erosion phenomenon can be simplified as the repeated impact of a single particle on the target material, resulting in the target material experiencing large stress-strain states during dynamic erosion. The simulation of particle impact dynamics in this paper is based on ABAQUS software due to its excellent ability to calculate nonlinear mechanics. Fig. 4 provides the schematic representation of the erosion model along with the corresponding computational mesh. The target material was set to a geometric size of  $1000 \mu\text{m} \times 1000 \mu\text{m} \times 500 \mu\text{m}$ , and a spherical particle with a diameter of  $400 \mu\text{m}$  impacted and contacted the target surface in the initial state. A mesh-independence test was conducted to select the appropriate mesh size for simulation, and the comparison of the maximum Von Mises stress of target material with the six representative grids is summarized in Table 3. It can be noted that a maximum difference of 13.52% exists between M1 and M2, and a minimum difference of 0.92% is present between M5 and M6. Considering the balance of accuracy and CPU time saving, M5 was selected as the computational mesh to be employed in all simulations, in which the number of elements was 847728.

The target material utilized in this simulation was AISI 4135 steel, which was consistent with the material used in the experiment. The stress-stain relationship of the target material can be described by the CSA-Z662-15 (2015) model, which was proposed by the Canadian oil and gas pipeline standard and widely used as a material model to represent the elastic-plastic mechanical properties of pipe steel (Yang et al., 2022; Zhu and Leis, 2005; Liu et al.,

2016; CSA-Z662-15, 2015). This model is a simple elastic-plastic, strain-hardening and strain-rate-hardening model that can be used to meet the needs of advanced dynamic simulations and dynamic material characterization, such as the erosion of high-speed particles. The mathematical expression of CSA-Z662-15 model is shown in Eqs. (2) and (3).

$$\varepsilon = \frac{\sigma}{E} + \left(0.005 - \frac{\sigma_y}{E}\right) \left(\frac{\sigma}{\sigma_y}\right)^{n^*} \quad (2)$$

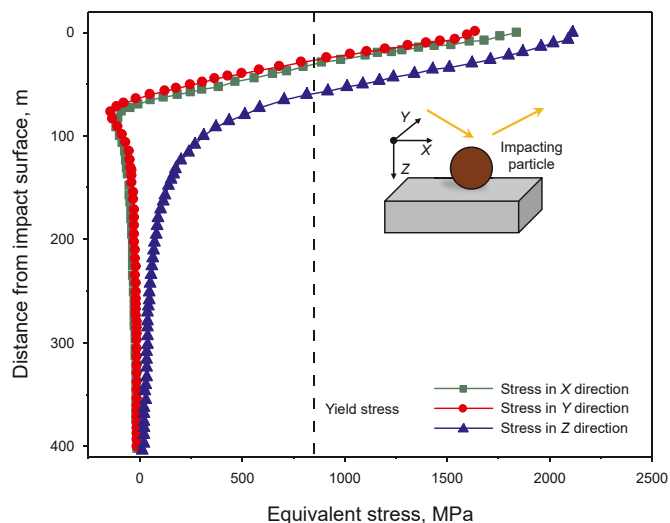
$$n^* = \frac{3.14}{1 - \frac{\sigma_y}{\sigma_t}} \quad (3)$$

where  $\varepsilon$  and  $\sigma$  represent strain and stress respectively;  $\sigma_y$  and  $\sigma_t$  represent yield stress and tensile stress respectively, which can be seen in Table 1 of the manuscript;  $E$  represents elastic modulus, which is  $2.07 \times 10^6$  MPa;  $n^*$  denotes the material hardening coefficient.

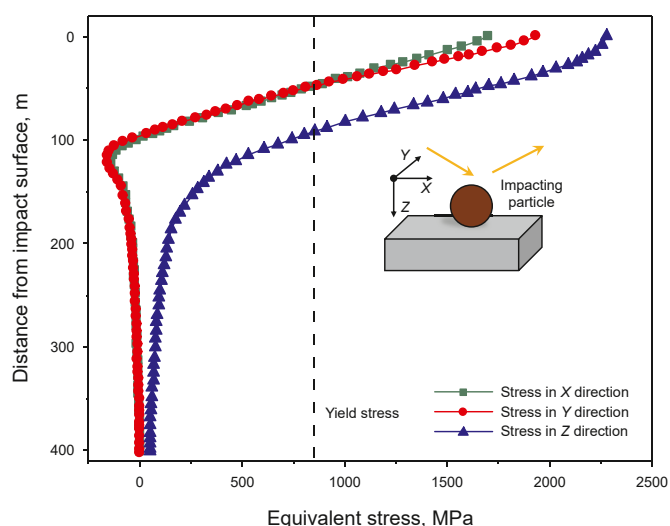
In the present study, erosion phenomenon is considered as the repeated impact of particles on the target surface, resulting in erosion damage of target material. Johnson-Cook damage model can be used to describe the complex failure behavior of the target material under particle impact, which comprehensively considers the effects of mechanical hardening, viscous strain rate and thermal softening (Johnson and Cook, 1985). The mathematical expression of Johnson-Cook model is shown in Eq. (4).

$$e^{\text{pl}} = \left(d_1 + d_2 e^{d_3(\sigma_p/\sigma_e)}\right) (1 + d_4 \ln \varepsilon) (1 + d_5 t) \quad (4)$$

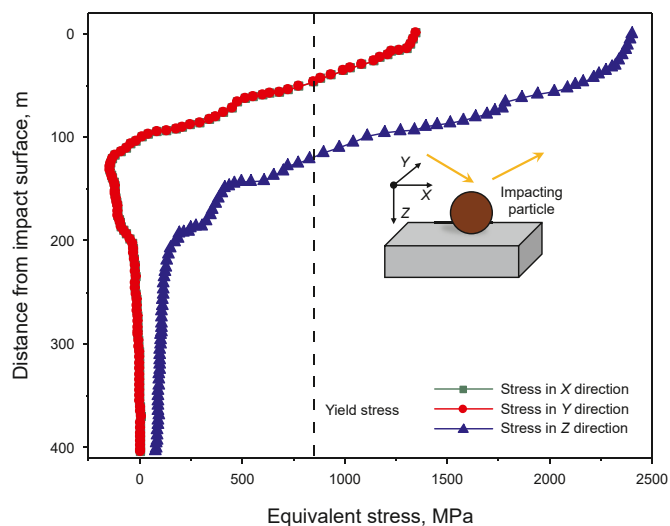
where  $e^{\text{pl}}$  is the equivalent plastic strain rate;  $\sigma_p$  and  $\sigma_e$  represent principal stress and equivalent stress respectively;  $t$  represents the material temperature; according to the experimental results in related literature (Wang et al., 2017),  $d_1$ – $d_5$  are empirical constants



(a) Impact angle = 30°



(b) Impact angle = 60°



(c) Impact angle = 90°

with values of  $d_1 = 0.35$ ,  $d_2 = 2.67$ ,  $d_3 = 4.33$ ,  $d_4 = 0.02$ , and  $d_5 = 1.6$ .

## 4. Results and discussion

### 4.1. Effect of impact angles on erosion

Fig. 5 depicts the erosion wear rate of the specimens at different impact angles. The flow velocity was set to 15 m/s and the specimens were not subjected to applied stress. It is evident that the erosion rate increased as the impact angle increased from 15° to 30°, reaching a maximum value at an impact angle of 30° ( $4.994e-03$  mg/g). The erosion wear rate was then noted to decrease gradually until the impact angle reached 90° ( $2.551e-03$  mg/g).

Fig. 6 displays the SEM micrographs of the eroded region of the target material at different impact angles. At low impact angles of 15° and 30°, the entire region was covered with narrow furrows. The lips observed on both sides and the front end of the furrows were essentially metal accumulations caused by particle extrusion. These fragile lips can be prone to reach critical strain hardening under the repeated impacts of subsequent particles, leading to detachment from the material surface. The furrows formed at an impact angle of 30° were shorter but deeper than those formed at an impact angle of 15°. At the intermediate impact angle of 60°, the furrows generated by the oblique impact of solid particles became significantly shorter compared to those at lower angles. In addition, the number of furrows decreased sharply, accompanied by some indentation craters. At the high angle impact of 90°, a ridge-like metal build-up can be formed around the indentation craters due to repeated vertical impacts and crushing of the impacting particles. Under successive particle impacts, micro-cracks tended to appear on the accumulated metal, which may be gradually developed and interconnect, leading to the formation of lamellar fragments that may then be dislodged under subsequent particle impacts.

In order to analyze the mechanical behavior during the evolution of erosion wear, we carried out particle impact dynamics simulations at different impact angles. Fig. 7 illustrates the equivalent contact stress nephograms of the surface and sub-surface of target material at three impact angles (30°, 60° and 90°). Upon the particle's contact with the target material, the stress on the worn surface would radiate in an approximately circular pattern in the subsurface layer beneath the contact surface. The stress level decreased gradually with the distance from the contact surface, and the maximum stress occurred in the contact area where the target material was impacted by the particle. The impact process of a solid particle on the target material was very short. At the initial moment, the particle impacted the target material, after which the worn surface started to be subjected to contact stress. For different impact angles, at the impact angles of 30° and 60°, the stress-affected area inclined in the direction of the horizontal component of the impacting particle's movement. However, at an impact angle of 90°, the stress-affected area was symmetrical due to the horizontal component of impact velocity of the particle was zero.

The distribution of equivalent contact stress in XYZ directions for different impact angles is shown in Fig. 8. The equivalent stress was found to be extremely high in the near-surface region, exceeding the yield strength of the material, indicating the possibility of fracture damage in this region. At an impact angle of 30°, the kinetic energy component in the X direction caused the particle to plow over the material surface, resulting in relatively large contact stress

Fig. 8. Variations in equivalent stress of target material at different impact angles (flow velocity = 15 m/s, applied stress = 0 MPa).

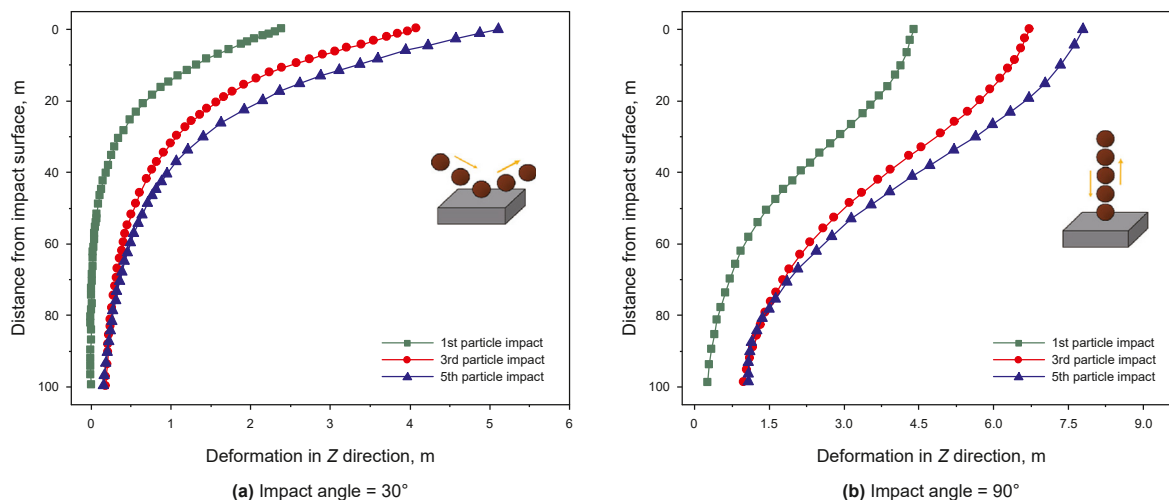


Fig. 9. Erosion deformation of the target materials under different particle impact times.

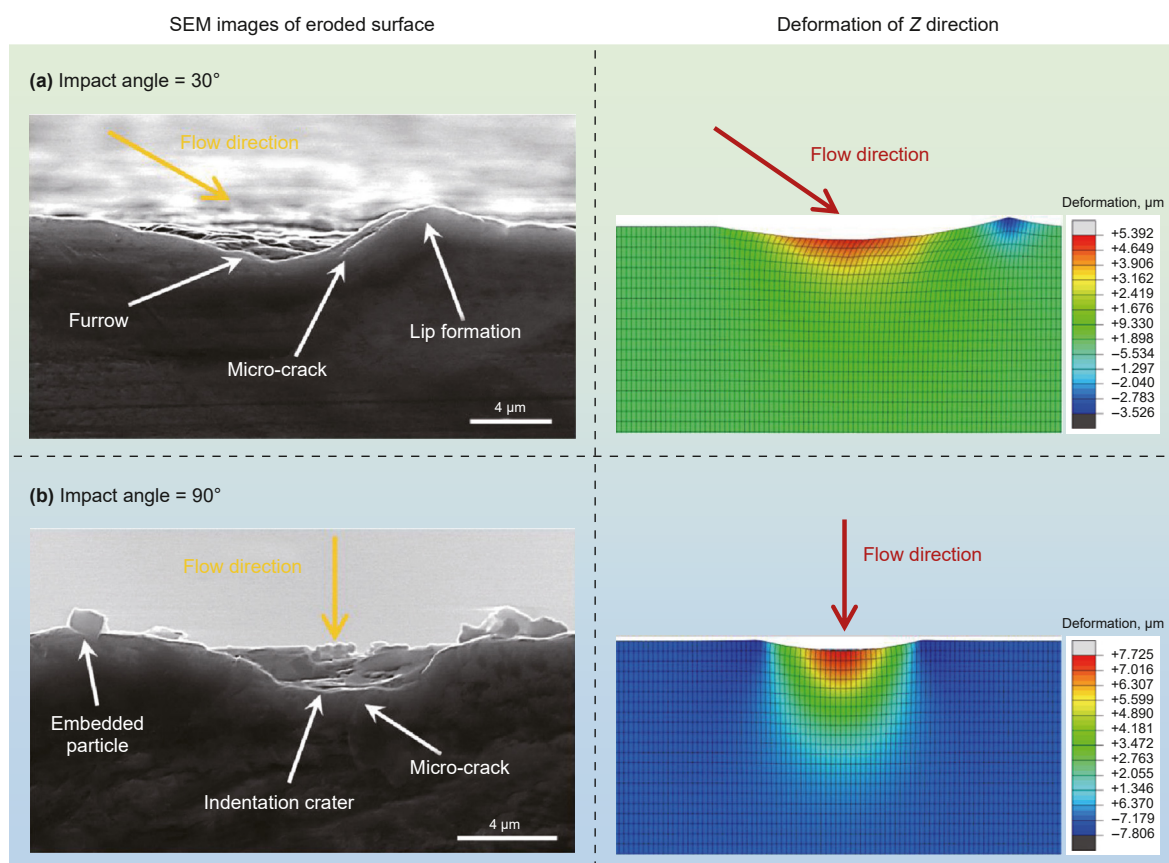
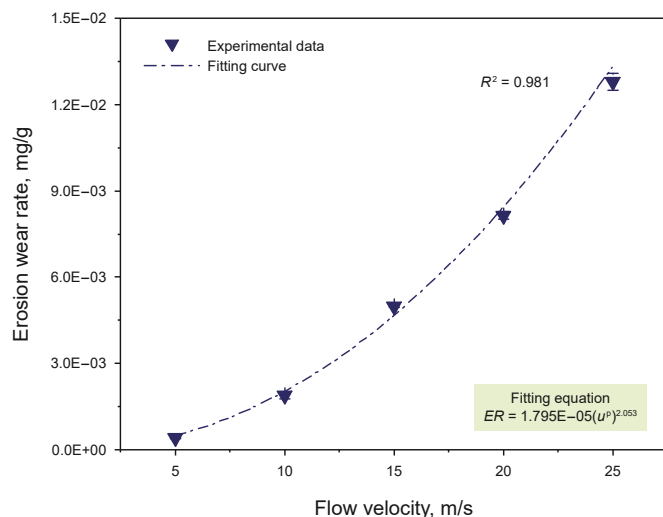


Fig. 10. Comparison of SEM micrographs and deformation nephograms of cross-section of the target materials.

in the horizontal direction of the target material. This led to plastic flow of metal on the target surface along the flow direction, resulting in the formation of narrow furrows (as shown in Fig. 6(b)). Combining the micrographs of the erosion area and the micro-mechanical analysis, it can be inferred that at the low angles (impact angle  $\leq 30^\circ$ ), the failure mode of erosion wear was mainly micro-cutting. Compared to the  $15^\circ$  impact, the  $30^\circ$  impact results in a shorter length of the furrow, but a significant increase in depth. At an impact angle of  $60^\circ$ , the contact stress decreased in the X

direction but increased in the YZ directions, resulting in a weakening of the furrows and a gradual appearance of indentation craters on the surface (as shown in Fig. 6(c)). Therefore, at the medium impact angles ( $30^\circ < \text{impact} \leq 60^\circ$ ), the erosion mechanism varied from micro-cutting to plastic deformation with the increase in impact angle. The erosion rate of the target material gradually decreases as the impact angle increases, which may be due to the more significant surface work-hardening effect with increasing plastic deformation. At the high impact angles, although



**Fig. 11.** Erosion rates at different flow velocities (impact angle = 30°, applied stress = 0 MPa).

the increase in the vertical kinetic energy component at higher impact angles leads to an increase in the contact stress of the target material in the Z direction, the contact stress of the target material in the XY direction gradually decreases. At an impact angle of 90°, the contact stress in the Z direction reached the maximum value and was much higher than that in the XY directions. In this case, the plastic deformation of the target material due to plastic extrusion dominated the failure mode of erosion wear, resulting in the disappearance of furrows and the entire eroded area being covered by indentation craters (as shown in Fig. 6(d)). In this case, the erosion rate of the target material reaches a minimum.

Erosion wear is characterized by the accumulation of damage resulting from repeated particle impacts on the target material. In the present study, we investigated the synergistic effect of multiple particles impacts on erosion wear. Fig. 9 illustrates the erosion deformation of the target material in the Z direction for different particle impact times at 30° and 90° impact angles. It can be seen that the deformation of the target material gradually increased as the number of particle impacts increased. In addition, the SEM micrographs of the cross-section of the eroded specimens and the corresponding deformation nephograms were obtained, as shown in Fig. 10. It can be seen from the comparison figures that the microstructural characterizations at two typical impact angles were in good agreement with the simulation results. As previously discussed, the failure modes dominating the erosion wear at 30° and 90° impact angles were different. Specifically, the low-angle

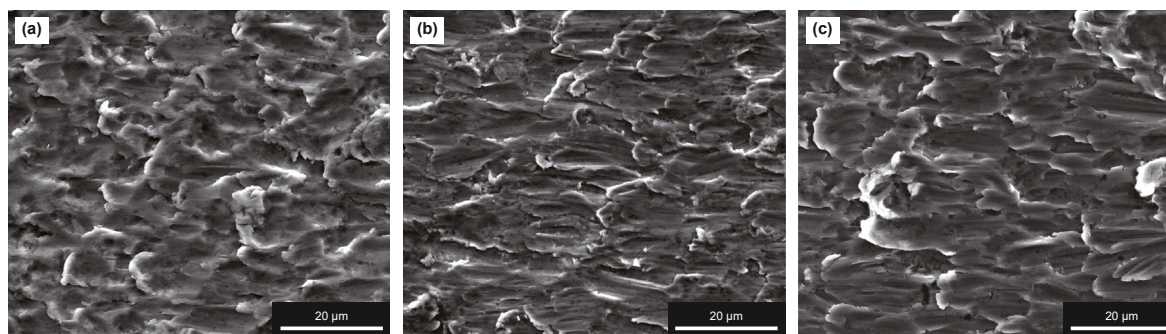
impacting particles induced micro-cutting, leading to the formation of furrows in the erosion region, and the accumulation of metal resulted in the formation of a lip in front of the furrow. In contrast, the high-angle impacting particles induced plastic extrusion, leading to the formation of indentation craters in the eroded region.

#### 4.2. Effect of flow velocities on erosion

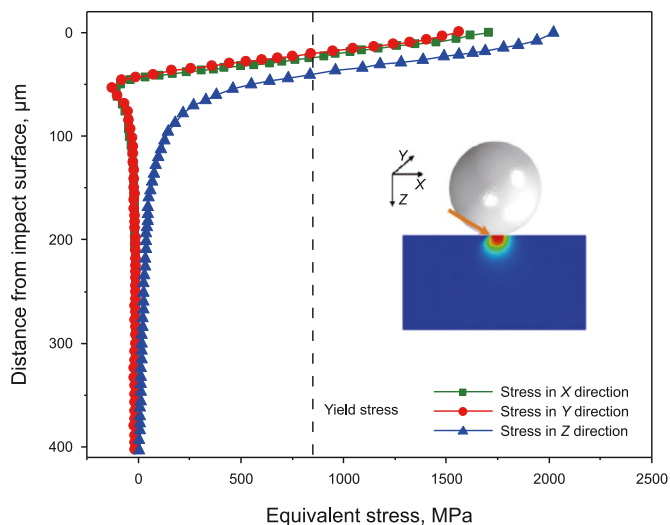
During the hydraulic fracturing, the flow velocity of fracturing fluid varies greatly with different operation stages. We conducted the erosion wear experiments involving different slurry flow velocities to investigate the effect of flow velocities on erosion severity of pipe steal for hydraulic fracturing. Fig. 11 shows the variety of erosion wear rate with flow velocity. The impact angle was set to 30° and the specimens were not subjected to applied stress. It can be clearly demonstrated that the effect of flow velocity on the erosion wear was significant, and the erosion wear rate increased rapidly with the increase of flow velocity. The relationship between erosion wear rate and flow velocity can be fitted by a power function, and the value of the power exponent was 2.053, which was consistent with the corresponding value for ductile metals.

Fig. 12 shows the SEM micrographs of the eroded region of the target material at different flow velocities, the impact angle was set to 30°. The eroded surface can be observed covered with furrows at different flow velocities. At a low flow velocity of 10 m/s, the size of the furrows was relatively small (see Fig. 12(a)). With the increase of flow velocity, the impacting particles have higher kinetic energy. As a result, when the particles with a higher flow velocity ploughed through the specimen surface, the sliding distance of the abrasive particles was longer, and the penetration depth was deeper. Thus, it was clearly evident that particles with higher flow velocity caused longer and deeper furrows. From the variety of the microstructure of eroded region at different flow velocities, it can be inferred that higher flow velocities lead to more severe erosion wear, which is consistent with the erosion test results.

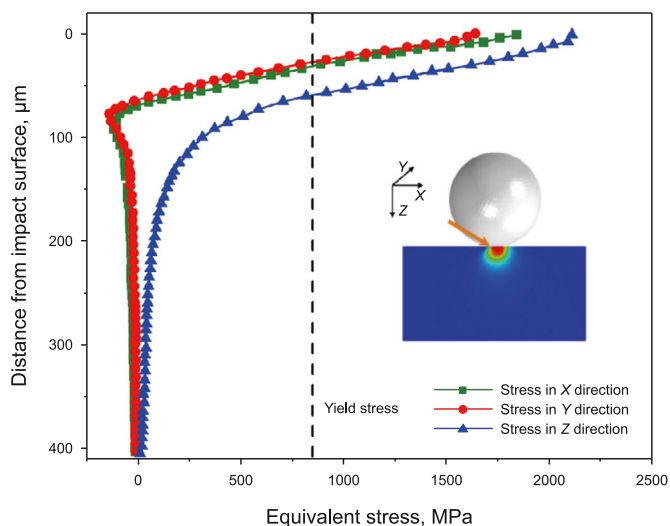
Fig. 13 shows the equivalent contact stress nephograms and distribution of equivalent contact stress of the target material at different impact velocities (10, 15 and 20 m/s). From the distribution of equivalent contact stress of the target material in the XYZ directions at three impact velocities, it can be seen that with the increase of impact velocity, the value and influence range of the equivalent contact stress of the target material in all three directions gradually increased. Accordingly, the volume deformation area of the target material increased due to the increase of the contact stress level and the influence range. Therefore, the higher velocity particle impacting the material surface can plow a longer distance and form a deeper furrow, which can be confirmed from



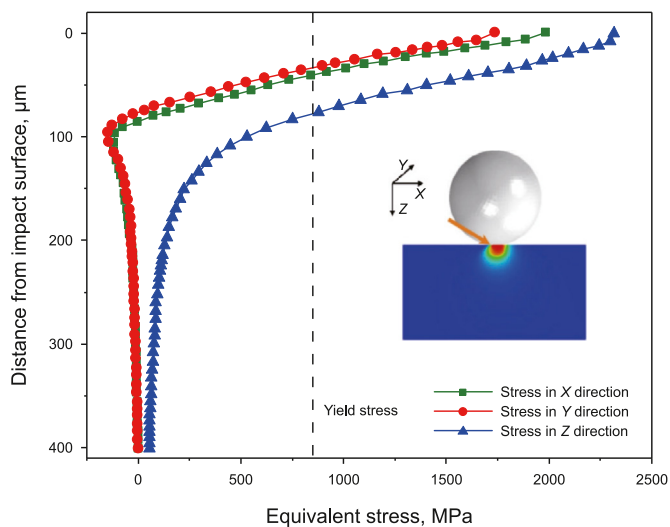
**Fig. 12.** SEM micrographs of the eroded region at different flow velocities. (a) Flow velocity = 10 m/s, (b) flow velocity = 15 m/s, (c) flow velocity = 20 m/s (impact angle = 30°, applied stress = 0 MPa).



(a) Impact velocity = 10 m/s



(b) Impact velocity = 15 m/s



(c) Impact velocity = 20 m/s

Fig. 13. Variations in equivalent stress of target material at different impact velocities (impact angle = 30°, applied stress = 0 MPa).

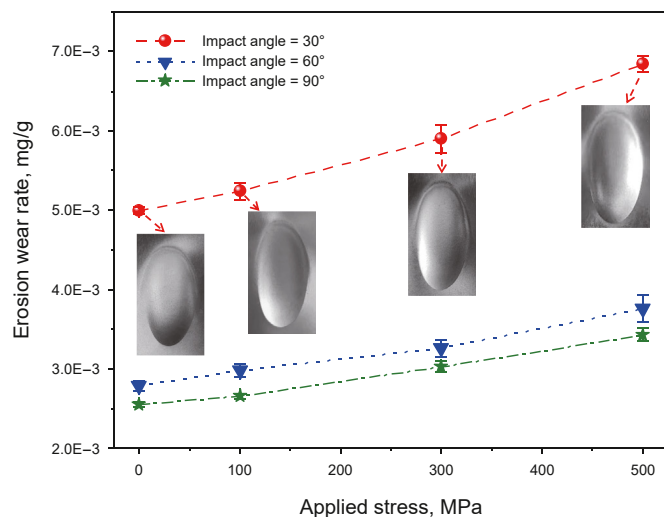


Fig. 14. Erosion rates at different applied stress (impact angle: 30°–90°, flow velocity: 15 m/s).

the SEM micrographs (see Fig. 12). In addition, the contact time between the particle and the target material decreased with the increase of the impact velocity. Therefore, an increase in impact velocity may result in more particles causing erosion damage to the target material in the same time. According to the relevant research of Hutchings (1981), in the process of particle impact target material, about 85%–90% of the particle kinetic energy gradually transforms into internal energy, resulting in the plastic deformation of target material. Moreover, about 1%–5% of the particle kinetic energy transforms into elastic wave energy, so that the bouncing particles can only retain about 1%–10% of the initial kinetic energy. Therefore, the impact particles with higher velocity consume more kinetic energy during the erosion, thus causing more serious erosion wear on the target material. From this, it can be concluded that the impact particles with higher velocity consume more kinetic energy during the erosion, thus causing more serious erosion wear on the target material. By analyzing the erosion mechanism at different particle impact velocities, the strong correlation between impact velocity and erosion severity can be well explained.

### 4.3. Effect of applied stress on erosion

During hydraulic fracturing, the fracturing pipes are inevitably subject to high stress caused by the high-pressure condition. Fig. 14 shows the variation of erosion wear rate at different applied stress. The flow velocity was set to 15 m/s and the impact angle was set to 30°, 60° and 90°. It can be seen from the figure that the erosion wear rate increased significantly with increasing applied stress. Compared with other angles, the increase in erosion wear rate with increasing stress level was most pronounced at the impact angle of 30°. This exacerbating effect of the applied stress on erosion wear may explain why fracturing pipes under high pressure are more prone to erosion damage than the normal pressure pipes. Therefore, the high internal pressure of in-service fracturing pipes would lead to a reduction in the erosion resistance of the pipe wall, resulting in more serious erosion wear. In addition, stress concentration exists in the erosion wear area of the pipe fitting, leading to further severe erosion wear of the fracturing pipes.

In order to analyze the erosion mechanism under different stress states, the SEM micrographs of eroded area of the target material at different applied stress were obtained, as shown in Fig. 15. It can be seen that there was a significant difference in the

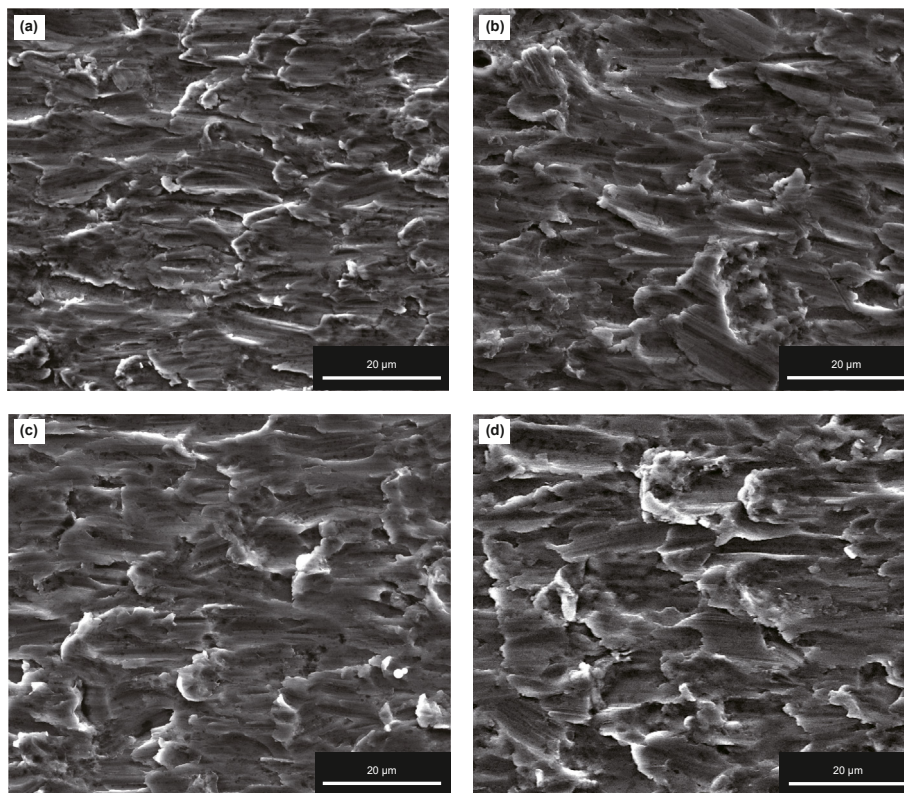


**Fig. 15.** SEM micrographs of the eroded region at different applied stress. (a) Applied stress = 0 MPa, (b) applied stress = 100 MPa, (c) applied stress = 300 MPa, (d) applied stress = 500 MPa (impact angle = 30°, flow velocity = 15 m/s).

microstructure of the target material in the eroded area with and without the applied stress. After the application of external tensile stress, the furrows generated by particles impact in the eroded area became more obvious, and it can be observed that the width and depth of the furrows gradually increased with the applied stress. From these microstructure properties, it can be inferred that the erosion resistance of the material decreased with the increase of the applied stress.

Furthermore, the particle impact dynamics simulations involving applied stress were carried out to analyze in detail the erosion mechanism with the consideration of stress state from the perspective of micromechanics. Based on the experimental conditions, the target material was subjected to the tensile stress along the Y direction when the particle impacted. In the erosion process, the particle impact angle was set to 30° and the impact velocity was set to 15 m/s. Figs. 16 and 17 show the deformation nephograms of the surface and sub-surface of target material in Y direction and Z direction under different stress levels, respectively. It can be seen from these figures that as the applied stress increased, the width and depth of the furrows caused by particle impact gradually increased, which was consistent with the microstructure characteristics reflected by the SEM micrographs (Fig. 15).

Figs. 18 and 19 show the distribution of erosion deformation of the target material in Y direction and Z direction under different stress, respectively. It can be seen from Fig. 18 that the metal near the center of the target material was squeezed to both sides under particle impact, and the value and range of the erosion deformation increased significantly with the increase of applied stress. Therefore, the width of the furrow formed by single particle impact was relatively large under high applied stress. In addition, it can be seen from Fig. 19 that the surface and sub-surface of the target material were displaced downward under particle impact, and the resulting

erosion pit depth increased significantly with the increase of applied stress. According to the SEM micrographs and micro-mechanical analysis of eroded area of the target material at different applied stress, it can be inferred that under the combined action of particle impact and applied stress, the influence region under multiple-stress was formed at the intersection of particles and target material. In this region, the stress state can be analyzed based on the rheological spring-slider theory (Dowling, 2012; Iwan, 1967). When particles impact, the plastic strain occurred in the metal due to slip transmission of grain boundaries. Interestingly, the plastic strain of elements in this region increased with the applied stress, resulting in an increase in the volume deformation of the target material. This explains why the size of the furrows increased evidently with a rise in stress levels under the action of stress-erosion. Therefore, it can be deduced that when the specimen was in a higher tensile stress state, the particles impinging on the target material can penetrate the surface more easily, leading to a decrease in the erosion resistance of the material with increasing applied stress.

## 5. Conclusions

The aim of this study was to reveal the erosion mechanism of pipe steel for hydraulic fracturing under the high-stress and multiphase flow coupling conditions. A series of erosion tests were carried out on AISI 4135 steel, and the effects of impact angle, flow velocity and applied stress on erosion wear were investigated comprehensively. Then the numerical simulations of particle impact dynamics were conducted. By combining the experimental studies and numerical simulations, the erosion mechanism of pipe steel under fracturing conditions were analyzed in detail. The following conclusions can be drawn.

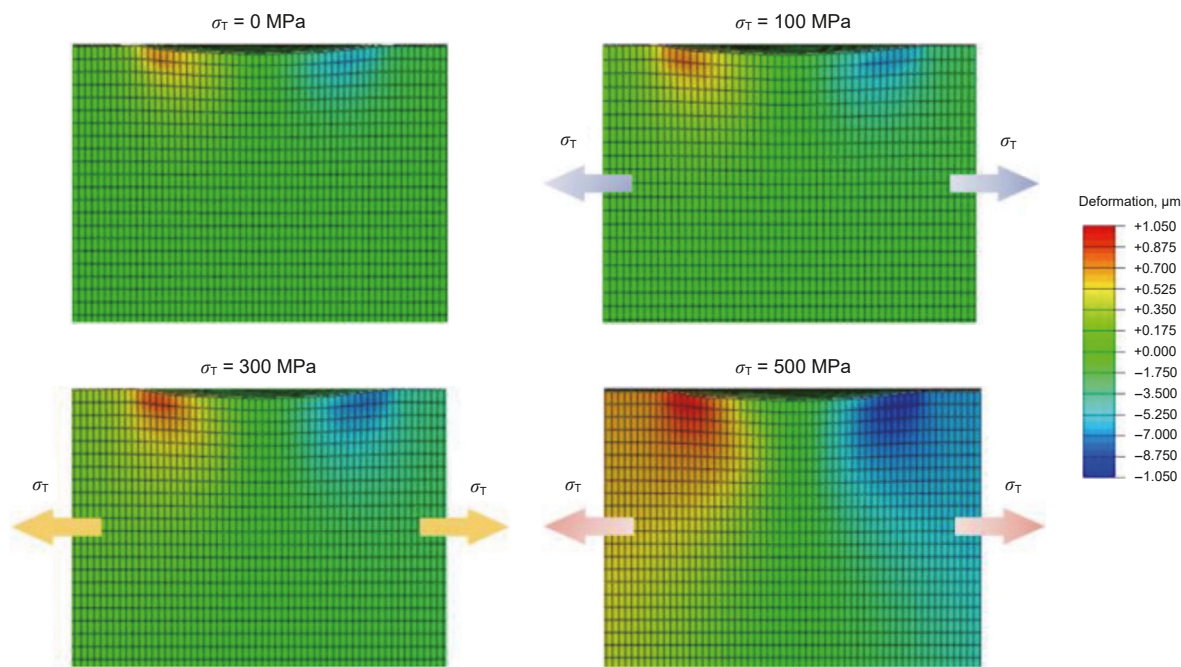


Fig. 16. Deformation nephograms of target material under different stress in Y direction (impact angle = 30°, flow velocity = 15 m/s).

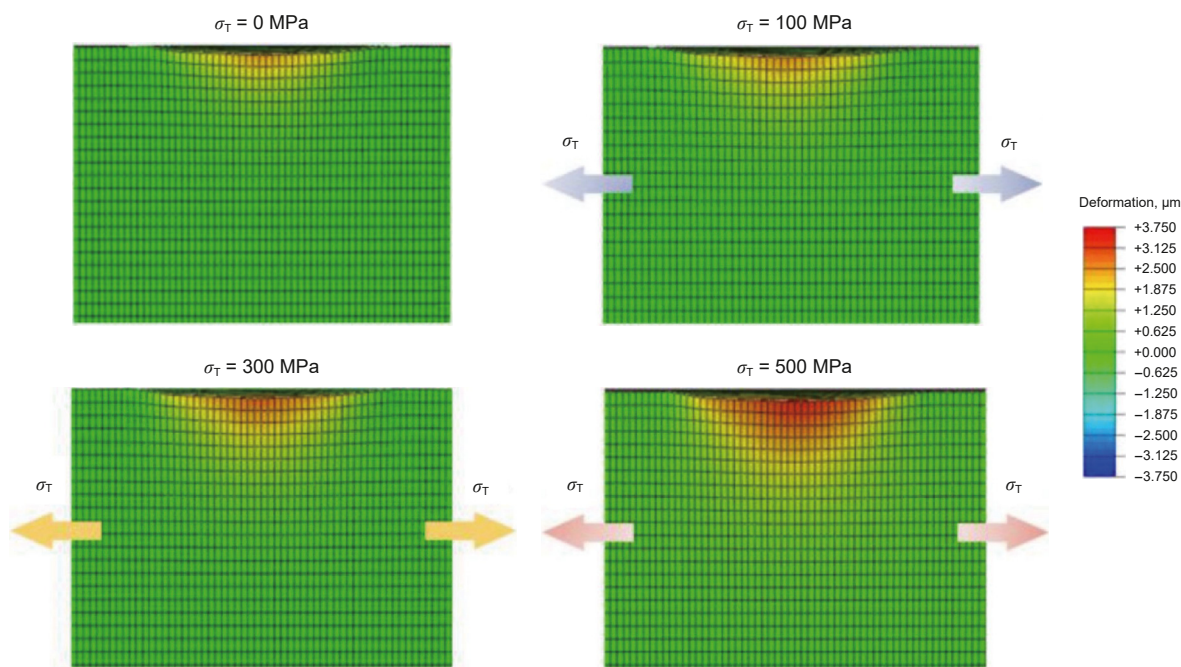
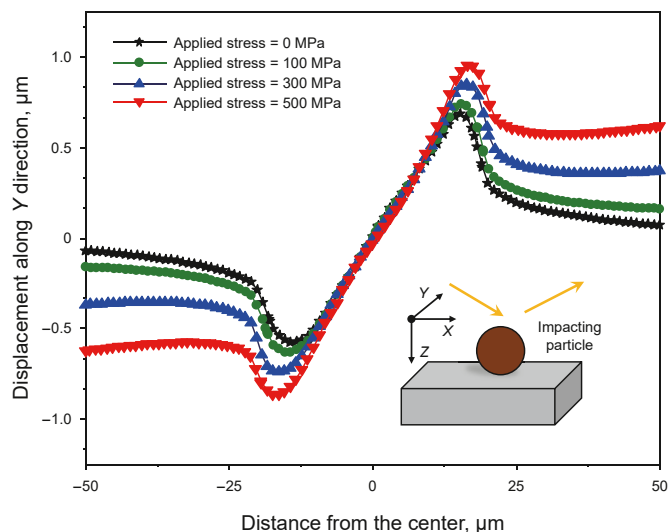


Fig. 17. Deformation nephograms of target material under different stress in Z direction (impact angle = 30°, flow velocity = 15 m/s).

(1) Based on the erosion experimental results, the varieties of erosion wear rates of AISI 4135 steel with three critical influencing factors under fracturing conditions were obtained. The erosion rate increased first and then decreased with the increase of impact angle, and the maximum and minimum erosion rates occurred at 30° and 90° impact angles. With the increase of flow velocity, the erosion rate increased as a power function. Moreover, the erosion rate was observed to increase significantly with the applied stress increased when other conditions remain unchanged, indicating that the erosion resistance of fracturing

pipes may be weakened under high-pressure operation condition.

(2) A particle impact dynamic model of erosion wear was developed according to the experimental parameters. Then the evolution process of particle erosion under different impact angles and impact velocities was analyzed. After the target material was impacted by the particle, a contact stress affected zone with approximate circular shape appeared. With the change of the impact angle, the components of the contact stress at target material changed greatly, resulting in a large



**Fig. 18.** Erosion deformation of the target materials under different applied stress in Y direction (impact angle = 30°, flow velocity = 15 m/s).

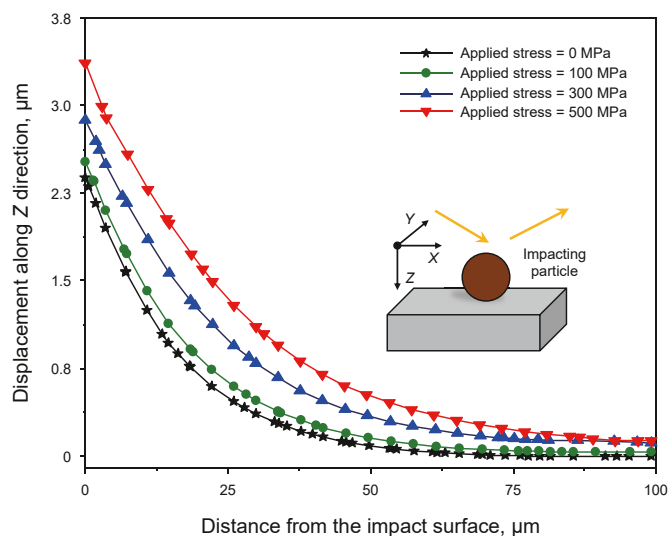


**Fig. 19.** Erosion deformation of the target materials under different applied stress in Z direction (impact angle = 30°, flow velocity = 15 m/s).

difference in the microstructure of the eroded area. With the increase of solid particle impact velocity, the range and stress level of the contact stress affected zone increased significantly, which can explain the strong correlation between impact velocity and erosion wear.

(3) The erosion mechanism of the target material under the coupling effect of particle impact and applied stress has been studied for the first time from the perspective of micro-mechanical. Combined with the SEM micrographs and the deformation micro-mechanics of erosion damage, it can be concluded that the influence region under multiple-stress was formed at the intersection of particles and target material, and the width and depth of the furrows caused by particles impact gradually increased with the applied tensile stress. Through the revelation of the stress-erosion mechanism, it can be known that the erosion rate of the fracturing pipes is affected by the huge stress caused by the high internal pressure. It is worth noting that the external areas of the high-pressure elbows for

hydraulic fracturing suffer a relatively high erosion rate under the coupling of particle impacts and huge circumferential stress. Therefore, a pre-stressed state can be formed on the outside of the elbow to effectively reduce the erosion wear.

Noted that in hydraulic fracturing, the actual loads on fracturing pipelines may be pulsating, and the steel used for fracturing pipelines is subjected to fluctuating stress coupled with particles erosion. Therefore, in the future research, it is necessary to consider the erosion tests and finite element simulations involving fluctuating stress, and analyze the formation mechanism of erosion pits and possible fatigue cracks in this case from the micro-mechanical point of view.

### CRediT authorship contribution statement

**Si-Qi Yang:** Writing – review & editing, Writing – original draft. **Jian-Chun Fan:** Supervision, Resources, Methodology, Funding acquisition. **Ming-Tao Liu:** Data curation. **De-Ning Li:** Methodology. **Jun-Liang Li:** Formal analysis. **Li-Hong Han:** Validation, Supervision. **Jian-Jun Wang:** Formal analysis. **Shang-Yu Yang:** Investigation. **Si-Wei Dai:** Visualization. **Lai-Bin Zhang:** Supervision.

### Declaration of competing interest

The authors declare that they have no known competing financial interests or personal relationships that could have appeared to influence the work reported in this paper.

### Acknowledgements

This research is supported by the National Natural Science Foundation Project of China (No. 52175208), Scientific Research and Technology Development Project of CNPC (No. 2023ZZ11), Fundamental Research and Strategic Reserve Technology Research Fund Project of CNPC (No. 2023DQ03-03), Study on Key Technologies of Production Increase and Transformation of Gulong Shale Oil (2021ZZ10-04).

### References

- Abbade, N.P., Crnkovic, S.J., 2000. Sand-water slurry erosion of API 5L X65 pipe steel as quenched from intercritical temperature. *Tribol. Int.* 33, 811–816. [https://doi.org/10.1016/S0301-679X\(00\)00126-2](https://doi.org/10.1016/S0301-679X(00)00126-2).
- Abedini, M., Ghasemi, H.M., 2014. Synergistic erosion-corrosion behaviour of Al-brass alloy at various impingement angles. *Wear* 319, 49–55. <https://doi.org/10.1016/j.wear.2014.07.008>.
- Ahlert, K., 1994. Effects of Particle Impingement Angle and Surface Wetting on Solid Particle Erosion of AISI 1018 Steel. MS. Thesis, The University of Tulsa, Department of Mechanical Engineering.
- Akbarzadeh, E., Elsaadawy, E., Sherik, A.M., Papini, M., 2012. The solid particle erosion of 12 metals using magnetite erodent. *Wear* 282–283, 40–51. <https://doi.org/10.1016/j.wear.2012.01.021>.
- Alam, T., Islam, M.A., Farhat, Z.N., 2016. Slurry erosion of pipeline steel: effect of velocity and microstructure. *J. Tribol. Trans. ASME* 138 (2), 021604. <https://doi.org/10.1115/1.4031599>.
- Al-Bukhaiti, M.A., Ahmed, S.M., Badran, F.M.F., Emara, K.M., 2007. Effect of impingement angle on slurry erosion behaviour and mechanisms of 1017 steel and high-chromium white cast iron. *Wear* 262, 1187–1198. <https://doi.org/10.1016/j.wear.2006.11.018>.
- Cao, X., Xiong, N., Li, J., Xie, Z.Q., Zang, X.R., Bian, J., 2022. Experimental study on the erosion of pipelines under different load conditions. *Fluid. Dyn. Mater. Proc.* 18 (2), 233–241. <https://doi.org/10.32604/fdmp.2022.018505>.
- Chen, Q., Li, D.Y., 2003. Computer simulation of solid-particle erosion of composite materials. *Wear* 255, 78–84. [https://doi.org/10.1016/S0043-1648\(03\)00065-6](https://doi.org/10.1016/S0043-1648(03)00065-6).
- CSA-Z662-15, 2015. *Oil and Gas Pipeline Systems*. CSA Group, Toronto.
- Dowling, D.E., 2012. *Mechanical behavior of materials: engineering methods for deformation, Fracture, and Fatigue, 4th Edition*. Pearson Education Inc, New Jersey.
- Duarte, C.A.R., Souza, F.J.D., 2017. Innovative pipe wall design to mitigate elbow erosion: a CFD analysis. *Wear* 380–381, 176–190. <https://doi.org/10.1016/j.wear.2017.03.015>.

- Hadavi, V., Moreno, C.E., Papini, M., 2016a. Numerical and experimental analysis of particle fracture during solid particle erosion, Part I: modeling and experimental verification. *Wear* 356–357, 135–145. <https://doi.org/10.1016/j.wear.2016.03.008>.
- Hadavi, V., Moreno, C.E., Papini, M., 2016b. Numerical and experimental analysis of particle fracture during solid particle erosion, Part II: effect of incident angle, velocity and abrasive size. *Wear* 356–357, 146–157. <https://doi.org/10.1016/j.wear.2016.03.009>.
- Huang, C., Chiovelli, S., Mineev, P., Luo, J., Nandakumar, K., 2008. A comprehensive phenomenological model for erosion of materials in jet flow. *Powder Technol.* 187, 273–279. <https://doi.org/10.1016/j.powtec.2008.03.003>.
- Hutchings, I.M., 1981. A model for the erosion of metals by spherical particles at normal incidence. *Wear* 70 (3), 269–281. [https://doi.org/10.1016/0043-1648\(81\)90347-1](https://doi.org/10.1016/0043-1648(81)90347-1).
- Islam, M.A., Alam, T., Farhat, Z., 2016. Construction of erosion mechanism maps for pipeline steels. *Tribol. Int.* 102, 161–173. <https://doi.org/10.1016/j.triboint.2016.05.033>.
- Iwan, W.D., 1967. On a class of models for the yielding behavior of continuous and composite systems. *J. Appl. Mech.-T. ASME*. 34, 612–617. <https://doi.org/10.1115/1.3607751>.
- Javaheri, V., Porter, D., Kuokkala, V.T., 2018. Slurry erosion of steel-Review of tests, mechanisms and materials. *Wear* 408–409, 248–273. <https://doi.org/10.1016/j.wear.2018.05.010>.
- Jonhson, G.R., Cook, W.H., 1985. Fracture characteristics of three metals subjected to various strains, strain rates, temperatures and pressures. *Eng. Fract. Mech.* 21 (1), 31–48. [https://doi.org/10.1016/0013-7944\(85\)90052-9](https://doi.org/10.1016/0013-7944(85)90052-9).
- Josifovic, A., Roberts, J.J., Corney, J., Davies, B., Shtipton, Z.K., 2016. Reducing the environmental impact of hydraulic fracturing through design optimization of positive displacement pump. *Energy* 115, 1216–1233. <https://doi.org/10.1016/j.energy.2016.09.016>.
- Liu, X.B., Zhang, H., Li, M., Xia, M.Y., Zheng, W., Wu, K., Han, Y., 2016. Effects of steel properties on the local buckling response of high strength pipelines subjected to reverse faulting. *J. Nat. Gas Sci. Eng.* 33, 378–387. <https://doi.org/10.1016/j.jngse.2016.05.036>.
- Liu, Y.F., Zhao, Y.L., Yao, J., 2021. Synergistic erosion-corrosion behavior of X80 pipeline steel at various impingement angles in two-phase flow impingement. *Wear* 466–467, 203572. <https://doi.org/10.1016/j.wear.2020.203572>.
- McLaury, B.S., Shirazi, S.A., 2000. An alternate method to API RP 14E for predicting solids erosion in multiphase flow. *J. Energy Resour. Technol.* 122 (3), 115–122. <https://doi.org/10.1115/1.1288209>.
- Nguyen, Q.B., Nguyen, V.B., Lim, C.Y.H., Trinh, Q.T., Sankaranarayanan, S., Zhang, Y.W., Gupta, M., 2014. Effect of impact angle and testing time on erosion of stainless steel at higher velocities. *Wear* 321, 87–93. <https://doi.org/10.1016/j.wear.2014.10.010>.
- Oka, Y.I., Okamura, K., Yoshida, T., 2005. Practical estimation of erosion damage caused by solid particle impact. Part 1: effects of impact parameters on a predictive equation. *Wear* 259, 95–101. <https://doi.org/10.1016/j.wear.2005.01.040>.
- Parsi, M., Najmi, K., Najafifard, F., Hassani, S., McLaury, B.S., 2014. A comprehensive review of solid particle erosion modeling for oil and gas wells and pipelines applications. *J. Nat. Gas Sci. Eng.* 21, 850–873. <https://doi.org/10.1016/j.jngse.2014.10.001>.
- Parsi, M., Agrawal, M., Srinivasan, V., 2015. CFD simulation of sand particle erosion in gas-dominant multiphase flow. *J. Nat. Gas Sci. Eng.* 27 (2), 706–718. <https://doi.org/10.1016/j.jngse.2015.09.003>.
- Parsi, M., Kara, M., Agrawal, M., 2017. CFD simulation of sand particle erosion under multiphase flow conditions. *Wear* 376–377, 1176–1184. <https://doi.org/10.1016/j.wear.2016.12.021>.
- Sapate, S.G., RamaRao, A.V., 2003. Effect of erodent particle hardness on velocity exponent in erosion of steels and cast irons. *Mater. Manuf. Process.* 18 (5), 783–802. <https://doi.org/10.1081/AMP-120024975>.
- Shimizu, K., Noguchi, T., Seitoh, H., Muranaka, E., 1999. FEM analysis of the dependency on impact angle during erosive wear. *Wear* 233, 157–159. [https://doi.org/10.1016/S0043-1648\(99\)00174-X](https://doi.org/10.1016/S0043-1648(99)00174-X).
- Shimizu, K., Seitoh, H., Okada, M., Matsubara, E., 2000. FEM analysis of erosive wear. *Wear* 250, 779–784. [https://doi.org/10.1016/S0043-1648\(01\)00716-5](https://doi.org/10.1016/S0043-1648(01)00716-5).
- Sun, B.C., Fan, J.C., Wen, D., Chen, Y.Y., 2015. An experimental study of slurry erosion involving tensile stress for pressure pipe manifold. *Tribol. Int.* 82, 280–286. <https://doi.org/10.1016/j.triboint.2014.07.025>.
- Veritas, N., 2007. Recommended Practice RP-0501: Erosive Wear in Piping Systems.
- Wang, H.K., Yu, Y., Xu, Y., Zhang, S.J., Li, X.B., 2022. A simple approach for coarse particle stress-erosion test with experimental validation. *J. Mater. Eng. Perform.* 31, 5823–5836. <https://doi.org/10.1007/s11665-022-06623-9>.
- Wang, Q.L., Jia, B.B., Yu, M.Q., He, M., Li, X.C., Sridhar, K., 2020. Numerical simulation of the flow and erosion behavior of exhaust gas and particles in polysilicon reduction furnace. *Sci. Rep.* 10, 1909. <https://doi.org/10.1038/s41598-020-58529-y>.
- Wang, S., Huang, Y., Xiao, Z., Yu, L., Liu, H., 2017. A modified Johnson-Cook model for hot deformation behavior of 35CrMo steel. *Metals* 7 (9), 337. <https://doi.org/10.3390/met7090337>.
- Wang, H.K., Yu, Y., Yu, J.X., Wang, Z.Y., Li, H.D., 2019a. Development of erosion equation and numerical simulation methods with the consideration of applied stress. *Tribol. Int.* 137, 387–404. <https://doi.org/10.1016/j.triboint.2019.05.019>.
- Wang, Z.G., Zhang, J., Shirazi, S.A., Dou, Y.H., 2019b. Experimental and numerical study of erosion in a non-Newtonian hydraulic fracturing fluid. *Wear* 422–423, 1–8. <https://doi.org/10.1016/j.wear.2018.12.080>.
- Xu, W.P., Wang, H.K., Yu, Y., Sun, Z.Z., Li, H.D., Zhao, Y., Fu, Y.Q., 2022. Study on applicability of microgroove erosion mitigation method based on stress-erosion coupling simulation. *Tribol. Int.* 174, 107746. <https://doi.org/10.1016/j.triboint.2022.107746>.
- Yang, K.G., Gao, D.L., 2022. Numerical simulation of hydraulic fracturing process with consideration of fluid-solid interaction in shale rock. *J. Nat. Gas Sci. Eng.* 102, 104580. <https://doi.org/10.1016/j.jngse.2022.104580>.
- Yang, S.Q., Fan, J.C., Zhang, L.B., Sun, B.C., 2021. Performance prediction of erosion in elbows for slurry flow under high internal pressure. *Tribol. Int.* 157, 106879. <https://doi.org/10.1016/j.triboint.2021.106879>.
- Yang, Y., Liu, X., Yang, H., Fang, W., Chen, P., Li, R., Gao, H., Zhang, H., 2022. A Semi empirical regression model for critical dent depth of externally corroded X65 gas pipeline. *Materials* 15 (16), 5492. <https://doi.org/10.3390/ma15165492>.
- Yao, L.M., Liu, Y.X., Xiao, Z.M., Feng, Z.M., 2023. Investigation on tee junction erosion caused by sand-carrying fracturing fluid. *Tribol. Int.* 179, 108157. <https://doi.org/10.1016/j.triboint.2022.108157>.
- Yoganandh, J., Natarajan, S., Babu, S., 2013. Erosive wear behavior of nickel-based high alloy white cast iron under mining conditions using orthogonal array. *J. Mater. Eng. Perform.* 22, 2534–2541. <https://doi.org/10.1007/s11665-013-0539-6>.
- Zang, X.R., Cao, X.W., Zhang, J., Xie, Z.Q., Xiong, N., Darihaki, F., Bian, J., 2022. Investigation of surface damage of ductile materials caused by rotating particles. *Wear* 488–489, 204185. <https://doi.org/10.1016/j.wear.2021.204185>.
- Zhang, J.X., Kang, J., Fan, J.C., Gao, J.C., 2016. Research on erosion wear of high-pressure pipes during hydraulic fracturing slurry flow. *J. Loss Prev. Process. Ind.* 43, 438–448. <https://doi.org/10.1016/j.jlp.2016.07.008>.
- Zhang, W.G., Zhang, S., Dai, W.H., Wang, X.Q., Liu, B.C., 2021. Erosion wear characteristics of cemented carbide for mud pulser rotor. *Int. J. Refract. Met. H.* 101, 105666. <https://doi.org/10.1016/j.ijrmhm.2021.105666>.
- Zhang, X., Zhang, L.B., Hu, J.Q., 2019. Real-time risk assessment of a fracturing manifold system used for shale-gas well hydraulic fracturing activity based on a hybrid Bayesian network. *J. Nat. Gas Sci. Eng.* 62, 79–91. <https://doi.org/10.1016/j.jngse.2018.12.001>.
- Zhang, Y., Reuterfors, E.P., McLaury, B.S., Shirazi, S.A., Rybicki, E.F., 2007. Comparison of computed and measured particle velocities and erosion in water and air flows. *Wear* 263, 330–338. <https://doi.org/10.1016/j.wear.2006.12.048>.
- Zhu, H.J., Wang, J., Ba, B., 2015. Numerical investigation of flow erosion and flow induced displacement of gas well relief line. *J. Loss. Prevent. Proc.* 37, 19–32. <https://doi.org/10.1016/j.jlp.2015.06.015>.
- Zhu, H.J., Qi, Y.H., 2019. Numerical investigation of flow erosion of sand-laden oil flow in a U-bend. *Process. Saf. Environ.* 131, 16–27. <https://doi.org/10.1016/j.psep.2019.08.033>.
- Zhu, X.K., Leis, B.N., 2005. Plastic collapse assessment method for unequal wall transition joints in transmission pipelines. *J. Pressure Vessel Technol.* 127 (4), 449–456. <https://doi.org/10.1115/1.2043197>.